

A crystal engineering approach for rational design of curcumin crystals for Pickering stabilization of emulsions

*Original*

A crystal engineering approach for rational design of curcumin crystals for Pickering stabilization of emulsions / Del Duca, Giulia; Parisi, Emmanuele; Artusio, Fiora; Cali, Eleonora; Fraterrigo Garofalo, Silvia; Rosso, Chiara; Cauda, Valentina; Chierotti, Michele R.; Simone, Elena. - In: FOOD RESEARCH INTERNATIONAL. - ISSN 0963-9969. - 194:(2024), pp. 1-17. [10.1016/j.foodres.2024.114871]

*Availability:*

This version is available at: 11583/2992449 since: 2024-09-14T07:18:54Z

*Publisher:*

Elsevier

*Published*

DOI:10.1016/j.foodres.2024.114871

*Terms of use:*

This article is made available under terms and conditions as specified in the corresponding bibliographic description in the repository

*Publisher copyright*

(Article begins on next page)

# A crystal engineering approach for rational design of curcumin crystals for Pickering stabilization of emulsions

Giulia Del Duca<sup>1</sup>, Emmanuele Parisi<sup>1</sup>, Fiara Artusio<sup>1</sup>, Eleonora Cali<sup>1</sup>, Silvia Fraterrigo Garofalo<sup>1</sup>, Chiara Rosso<sup>2</sup>, Valentina Cauda<sup>1</sup>, Michele Remo Chierotti<sup>2</sup>, Elena Simone<sup>1\*</sup>

*Affiliations*

*1 Department of Applied Science and Technology (DISAT), Politecnico di Torino, 10129 Torino, Italy*

*2 Dipartimento di Chimica I.F.M, Università degli Studi di Torino, 10125, Torino, Italy*

*\*Corresponding author: elena.simone@polito.it*

**Keywords: crystal engineering, curcumin, Pickering, anti-solvent crystallization**

## Abstract

Emulsions stabilized via Pickering particles are becoming more and more popular due to their high stability and biocompatibility. Hence, developing new ways to produce effective Pickering particles is essential. In this work, we present a crystal engineering approach to obtain precise control over particle properties such as size, shape, and crystal structures, which may affect wettability and surface chemistry. A highly reproducible synthesis method via anti-solvent crystallization was developed to produce submicron-sized curcumin crystals of the metastable Form III, to be used as Pickering stabilizers. The produced crystals presented a clear hydrophobic nature, which was demonstrated by their preference to stabilize water-in-oil (W/O) emulsions. A comprehensive experimental and computational characterization of curcumin crystals was performed to rationalize its hydrophobic nature. Analytical techniques including Raman spectroscopy, powder X-ray diffraction (PXRD), Solid-State Nuclear Magnetic Resonance (SSNMR), scanning electron microscopy (SEM), Differential Scanning Calorimetry (DSC), confocal fluorescence microscopy and contact angle measurements were used to characterize curcumin particles in terms of shape, size and interfacial activity. The attachment energy model was instead applied to study relevant, surface properties of curcumin crystals, such as topology and facet-specific surface chemistry. This work contributes to the understanding of the effect of crystal properties on the mechanism of Pickering stabilization and

28 paves the way for the formulation of innovative products in fields ranging from pharmaceuticals to  
29 food science.

30

## 31 **Introduction**

32 Nowadays, emulsions are widely used in the food and pharmaceutical industries for encapsulation,  
33 controlled release, and delivery of active compounds (Chen et al., 2020; Frelichowska et al., 2009;  
34 Tan & McClements, 2021; Tang et al., 2015).

35 In recent years, there has been a growing interest in Pickering systems (Dickinson, 2010; Ewens et  
36 al., 2021; Metilli et al., 2022; Yang et al., 2017), a specific type of emulsion stabilized by solid  
37 particles, which irreversibly adsorb at the interface between two immiscible phases (Chevalier &  
38 Bolzinger, 2013). The use of solid particles to stabilize interfaces offers more appealing properties  
39 compared to synthetic surfactants (Binks, 2002); in fact, Pickering systems present lower tendency  
40 to coalescence of the dispersed phase, higher mechanical resistance and enhanced thermodynamic  
41 stability (Albert et al., 2019; Aveyard et al., 2003). Additionally, food-grade particles derived from  
42 natural sources can be used as stabilizers for food, pharmaceutical and agrochemical applications.  
43 Compared to traditional stabilizers food-grade, natural particles are more sustainable, less toxic,  
44 more biocompatible and are associated to less negative side effects like irritation and allergies (Tang  
45 et al., 2015).

46 The formation mechanism, thermodynamic stability, and functionality of Pickering emulsions are  
47 influenced by many factors, including particle wettability, size, and morphology (e.g., aspect ratio)  
48 distributions (Pugh, 2016; Wu & Ma, 2016; Xia et al., 2021). Therefore, a correct design of crystalline  
49 particles and the related production processes is crucial to obtain the desired multiphase system  
50 performance.

51 The type of emulsion stabilized by Pickering particles, whether oil-in-water (O/W) or water-in-oil  
52 (W/O), is influenced by the surface nature of Pickering particles. This is often described by the three-  
53 phase contact angle ( $\theta$ ) formed between the solid particle and the oil/water interface. When the  
54 angle formed on the water side ( $\theta_w$ ) is less than  $90^\circ$ , particles are more suitable for the stabilization  
55 of O/W emulsions. On the contrary, when this contact angle exceeds  $90^\circ$ , the formation of W/O  
56 emulsion is more favoured (Binks & Lumsdon, 2000).

57 The size distribution of Pickering particles also influences directly the average size of emulsion  
58 droplets formed during emulsification. Typically, Pickering particles are at least one order of  
59 magnitude smaller than the average size of emulsion droplets (Xia et al., 2021). Particle morphology  
60 (e.g., aspect ratio) was also found to have an effect on Pickering stabilization; particles characterized  
61 by a high value of aspect ratio, such as ellipsoids, fibres and rods, were found to better stabilize  
62 emulsion droplets compared to more spherical shapes (Jafari et al., 2020).

63 A variety of plant-derived particles, such as polysaccharides (e.g., cellulose, starch, chitosan),  
64 proteins, and polyphenol crystals (Luo et al., 2011), can be utilized to stabilize emulsions. Crystalline  
65 polyphenols, including curcumin, are particularly attractive due to their edibility, cost-effectiveness,  
66 and health benefits (Xiao et al., 2021). Curcumin is one of the most recently studied compounds  
67 (Nelson et al., 2017), which also exhibits surface activity (Sarkar & Dickinson, 2020; Zembyla et al.,  
68 2020)(Aditya et al., 2017; Zembyla et al., 2018, 2019). Furthermore, curcumin has a high tendency  
69 to arrange in different crystal structures, such as polymorphs or co-crystals (Sanphui & Bolla, 2018).  
70 Polymorphs and co-crystals of the same compound can present different bulk properties such as  
71 solubility, thermodynamic stability, and dissolution rate; but also different surface features (i.e.,  
72 roughness and chemical nature), which can be rationally linked with crystal structure properties  
73 (Klitou et al., 2022, 2023) (Prandini et al., 2024; Preston et al., 2024).

74 In this work, a crystal engineering approach was used to develop a robust methodology for the  
75 synthesis of sub-micron curcumin particles suitable for Pickering stabilization. In particular, crystal  
76 engineering tools such as molecular modelling (e.g., Particle Informatics) and multi-technique  
77 particle characterization techniques (e.g., SEM, DSC, XRD) were used to relate crystal structure with  
78 important Pickering properties such as roughness and surface chemistry (Desiraju, 2013).

79 Curcumin crystals were obtained by anti-solvent crystallization, a technique that offers better control  
80 over crystal size and shape distribution compared to classical top-down methodologies such as  
81 micronization (e.g., jet or ball milling). Additionally, anti-solvent crystallization prevents the  
82 formation of amorphous, unstable particles, (Thorat & Dalvi, 2012) and favours the growth of  
83 crystals with narrow size and shape distributions. On the other hand, anti-solvent crystallization  
84 processes make use of organic solvents, which usually needs to be separated from the anti-solvent  
85 (e.g., via distillation) after particles have formed. Additionally, this particle production technique  
86 requires further unit operations such as filtration or centrifugation to separate solid particles from  
87 the mother liquor.

88 Following another typical crystal engineering approach (Simone et al., 2015; Simone & Nagy, 2015),  
89 we performed a systematic investigation of the relationship between crystallization conditions (e.g.,  
90 stirring rate, ratio solvent to anti-solvent, volume and concentration) and curcumin crystal shape  
91 (aspect ratio), size and polymorphism using Design of Experiment (DoE). Finally, interfacial  
92 properties of curcumin crystals were studied with contact angle measurements, emulsification  
93 experiments and confocal fluorescence microscopy. This work highlights a clear relationship  
94 between crystal properties of curcumin particles (size, shape, polymorphic form) and their ability to  
95 act as Pickering stabilizer, showing that a crystal engineering approach can be effective in the design  
96 of Pickering particles and the processes necessary to produce them.

97

## 98 **1. Materials and Methods**

99 Curcumin from turmeric rhizome (98 wt% total curcuminoid content, >78 wt % curcumin) was  
100 obtained from Thermo Fisher Scientific. Ethanol (99.98%) was purchased from Sigma-Aldrich.  
101 Medium-chain triglycerides (MCT) oils (Nature Aid) was purchased from a local store. Water purified  
102 by treatment with a Milli-Q apparatus was used for all the experiments. The curcuminoid mixture  
103 was used without further purification and will be referred to as raw curcumin from now on in this  
104 paper. The presence of structurally related impurities (*Figure 1*) is not a limitation for the purpose of  
105 this work. Curcumin molecules in the crystal lattice mainly interact via hydrogen bonding  
106 interactions that do not involve the methoxy groups; these are not even involved in any significant  
107 intramolecular interaction that can be responsible for molecular torsion (Heffernan et al., 2018).  
108 Thus, the presence of a high concentration of demethoxycurcumin incorporated in the crystal  
109 structure does not greatly affect the properties of the powder.

### 110 **1.1 Solubility measurement in Ethanol**

111 The solubility of curcumin as purchased (Form I) in ethanol was determined using the Crystal 16  
112 apparatus (Technobis). Curcumin was previously gently ground in a mortar using an agate pestle,  
113 then weighed and dispersed in ethanol in a 1.5 mL vial. 12 different concentrations were prepared.  
114 Bottom stirring at a fixed speed of 780 rpm was used to keep the particles well dispersed. The  
115 samples underwent three consecutive dissolution and recrystallization cycles, by changing  
116 temperature from 0 °C to 70 °C, with a heating rate of 0.3 °C/min and a cooling rate of -0.3 °C/min.

117 **1.2 Solubility measurement in ethanol-water mixtures**

118 Raw curcumin in ethanol-water mixtures in different ratios was quantified with a high-performance  
119 liquid chromatography (HPLC) system (Shimadzu 20A Nexera). A Kinetex core shell C18 column (5  
120  $\mu\text{m}$ ,  $150 \times 4.6$  mm) by Phenomenex and a photo diode array detector were employed to quantify  
121 the solute dissolved in the mixtures. Curcumin and solvents absorbance was previously evaluated;  
122 425 nm wavelength was selected. The mobile phase used consisted of acetonitrile and 0.1% formic  
123 acid at a ratio of 50/50 (v/v). The analytes were eluted using a isocratic elution method with a flow  
124 rate maintained at 0.8 mL/min, and the column oven temperature fixed at 40 °C. The injection  
125 volume was set at 10  $\mu\text{L}$  (Peram et al., 2017). The calibration curve was obtained starting from a  
126 series of standard solutions of raw curcumin in ethanol with varying concentrations from 0.1  $\mu\text{g}/\text{mL}$   
127 to 100.0  $\mu\text{g}/\text{mL}$ , obtained by serial dilutions from the 100.0  $\mu\text{g}/\text{mL}$  ethanolic stock solution. A total  
128 of nine points were collected in duplicate. The quantification of curcumin dissolved in ethanol-water  
129 mixtures with increasing water content (ratio ranging from 1:2.5 to 1:20 w/w) was determined by  
130 interpolation from the calibration curve. The analyte composition of the solvent had no significant  
131 effect on the precision of the calibration method. The analyte samples were prepared stirring for 15  
132 minutes an excess of raw curcumin in the ethanol-water mixtures. . The excess precipitate was  
133 allowed to settle and the dispersions were filtered using a 22  $\mu\text{m}$  syringe filter. The resulting solutions  
134 were then placed in HPLC vials for quantification. The measurements were conducted in triplicate.

135 **1.3 Anti-solvent crystallization experiments**

136 Anti-solvent precipitation experiments were designed considering different operating conditions,  
137 namely the concentration of curcumin in the ethanolic solution, the ethanol-water ratio, the final  
138 volume of the crystallization solution, and the speed of stirring during the anti-solvent addition. A  
139 Design of Experiment (DoE) approach was used to plan a set of experiments varying these four  
140 different factors. Five different levels for each factor were considered (*Supporting Info Table S1*). The  
141 experimental matrix was generated using the default *ccdesign* function in MATLAB R2021a. A  
142 statistical analysis of the effect of these different experimental factors (and their combinations) on  
143 particle average size and aspect ratio was conducted using the Chemometric Agile Tool (CAT) 3.1.2  
144 software, freely available from <https://www.gruppochemiometria.it/f> following the approach  
145 shown by (Leardi, 2009).

Codice campo modificato

146 *Table 1* lists the conditions selected for each experiment. Raw curcumin was weighed and solubilized  
147 in ethanol (solvent). The curcumin ethanolic solution was then rapidly mixed with Milli-Q water (anti-  
148 solvent) at room temperature in a 1 L beaker in one step addition. While pouring the ethanolic  
149 solution, the water was stirred using an Ultra-Turrax (IKA) device to create homogeneous  
150 supersaturation. The mixture was stirred an additional 5 min to ensure equilibrium after the  
151 curcumin crystal precipitation. The resulting dispersion was filtered under vacuum using a Büchner  
152 flask, funnel, and filter paper (90 mm diameter) to separate the particles formed from the solvent  
153 mixture. The filter cake was washed with water and completely dried in open air for 24 hours. Both  
154 the curcumin raw material and curcumin recrystallized powders obtained (named curcumin  
155 recrystallized from now on in this paper) have been subjected to extensive characterization.

#### 156 **1.4 Characterization of curcumin crystals**

157 **Raman Microscopy:** To check the homogeneity of the curcumin recrystallized powders, Raman  
158 spectra and spatial maps were acquired at room temperature using a confocal Raman microscope  
159 Horiba LabRAM HR Evolution. A 785 nm laser was used as the excitation source, and the Raman  
160 signal was collected with a Synapse Plus BIDD Detector (1024 x256 pixels), utilizing a 300/nm grating.  
161 No filter was applied and the laser power was set at 50%. Several milligrams of material were placed  
162 on a glass slide, the powder was pressed and scanned in a grid pattern using the 5X objective. The  
163 sampling parameters were set to get 5 acquisitions with an exposure time of 0.5 s, and a total of 100  
164 points were measured for each sample.

165 To check the kinetic stability of the recrystallized powder in water, a total of 150 mg of recrystallized  
166 curcumin was dispersed in 200 mL of Milli-Q water in a 250 mL graduated jacketed reactor. The  
167 dispersion was maintained in agitation using magnetic stirring at 400 rpm for 63 hours. A Huber  
168 Ministat 230 (Huber, Germany) was used to control and maintain the temperature constant at 25 °C.  
169 The dispersion was monitored in situ using a fiber-optic SuperHead Raman probe, with a 785 nm  
170 laser as the excitation source, connected to the Horiba LabRam mentioned earlier. To prevent  
171 interference from external light, the slurry, and the probe were covered in aluminium foil. One  
172 spectrum was recorded every hour, to monitor possible changes in solid form. The acquisition  
173 parameters were set to collect 20 acquisitions with 10 s exposure time. The effects of cosmic rays in  
174 the spectra were manually removed.

175 **Powder X-ray Diffraction (PXRD):** PXRD analysis was performed using a Panalytical X'Pert PRO  
176 diffractometer set up in Bragg–Brentano mode with Cu K $\alpha$  radiation ( $\lambda = 1.5406 \text{ \AA}$ ). The samples  
177 were gently ground in a mortar with an agate pestle and loaded onto a silicon zero-background  
178 sample holder, and diffraction patterns were recorded over a  $2\theta$  range of  $4^\circ$  to  $40^\circ$  with a step size  
179 of  $0.026^\circ$  and an acquisition time of 180 seconds per step. The obtained diffraction patterns were  
180 compared with the simulated X-ray patterns obtained from the polymorphs crystal structures  
181 deposited in the Cambridge Structural Database (CSD), refcodes BINMEQ13, BINMEQ12 and  
182 BINMEQ07 for form I, II and III, respectively.

183 **Solid-State Nuclear Magnetic Resonance (SSNMR):**  $^{13}\text{C}$  CPMAS (*Cross-Polarization Magic Angle*  
184 *Spinning*) SSNMR spectra were acquired with a Bruker Avance II 400 Ultra Shield instrument,  
185 operating at 400.23 MHz for  $^1\text{H}$  and 100.63 MHz for  $^{13}\text{C}$ . The powder samples were packed into  
186 cylindrical zirconia rotors with a 4 mm o.d. and 80  $\mu\text{L}$  volume without further preparations or  
187 treatments.  $^{13}\text{C}$  spectra were acquired at room temperature at a spinning speed of 12 kHz using a  
188 ramp cross polarization (CP) pulse sequence with a  $90^\circ$   $^1\text{H}$  pulse of 3.8  $\mu\text{s}$ , a contact time of 3 ms,  
189 optimized recycle delays of 3.94 and 3.6 s for raw curcumin and the recrystallized sample  
190 respectively, and a number of scans equal to 1000. The two-pulse phase modulation (TPPM) scheme  
191 was used for heteronuclear decoupling, with a radio frequency field of 65.8 kHz. The  $^{13}\text{C}$  chemical  
192 shift scale was calibrated through the methyl signal of the external standard adamantane (at 38.48  
193 ppm with respect to tetramethyl silane, TMS).

194 **Differential Scanning Calorimetry (DSC):** DSC analysis was performed using a Mettler Toledo  
195 8000 DSC-1 calorimeter. Approximately 2.5 mg of each sample was placed in a 40  $\mu\text{L}$  aluminium pan,  
196 covered with a perforated lid. The samples were heated from  $25^\circ\text{C}$  to  $185^\circ\text{C}$  at a heating rate of 10  
197  $^\circ\text{C}/\text{min}$  under a nitrogen atmosphere and then cooled to  $20^\circ\text{C}$ , at a cooling rate of  $10^\circ\text{C}/\text{min}$ .

198 **Scanning Electron Microscopy (SEM):** The crystal morphology and particle size distribution of the  
199 recrystallized curcumin samples were assessed through image analysis obtained with a Zeiss Merlin  
200 Field Emission Gun Scanning Electron Microscope. Dry particles were finely dispersed using a spatula  
201 then fixed onto SEM specimen stubs. A platinum coating was deposited to improve sample  
202 conductivity for better image quality. The coating procedure lasted for 30 s at 30 mA. The acquired  
203 SEM images were subjected to analysis using ImageJ 1.54g software. Images were manually  
204 segmented. Binarization was applied to convert the images into binary format, and the dimensions  
205 (length and width) of the particles were obtained through the software. Due to the needle-like/rod-

206 shaped morphology of the particles, an ellipse was fitted to each particle (ImageJ default function  
207 “Fit ellipse”), and the minimum and maximum lengths were considered to calculate the aspect ratio  
208 and Feret’s diameter (called equivalent diameter from now on). An example of the workflow used  
209 for image analysis is shown in *Supporting Info Figure S1*. To ensure statistical reliability, a minimum  
210 of 300 particles were selected for each sample as shown in *Supporting Info Table S2*.

### 211 **1.5 Computational analysis of curcumin crystal structures**

212 The crystallographic information files (.cif) for the two curcumin polymorphs structures (form I and  
213 form III) used in the analysis were obtained from the Cambridge Structural Database (CSD), refcode  
214 BINMEQ13 for form I, refcode BINMEQ07 for form III. The .cif files were analyzed with the CCDC  
215 Mercury software v.2023.1.0 (Macrae et al., 2008). The optimization of the crystal structures was  
216 performed using Materials Studio 2021 (v 21.1.1.3268). Geometry optimization was carried out with  
217 the Forcite algorithm with Dreiding force field (Liu et al., 2019). The crystal habit of the curcumin  
218 polymorphs was predicted by the growth morphology method, which gave several possible crystal  
219 faces. The crystals were sliced parallel to the morphologically important surfaces (h k l) with a depth  
220 of  $2 \times dhkl$ . A crystal segment was created as a periodic superstructure of  $3 \times 3$  unit cells. The  
221 interactions between the molecules in the unit cell were calculated with the Crystal Graph tool of  
222 the morphology module in Material Studio that ranks the intermolecular interactions. Thus, the  
223 fastest growth rate of the crystal surface would be present in the direction that contains the  
224 strongest interactions, which means that the curcumin molecules grow faster along the strongest  
225 interaction. The crystal surfaces that have a fast growth rate will vanish and the crystal surfaces with  
226 a slow growth rate will appear in the final morphology. The surface analysis of the crystal facets of  
227 the two polymorphs was performed with CSD-particle tool in Mercury to study the surface  
228 roughness of the most dominant facets.

### 229 **1.6 Contact Angle Measurements**

230 The wettability of both the raw curcumin and the crystallized particles was evaluated by measuring  
231 the contact angle through sessile drop technique using a DSA25 Drop Shape Analyzer (Krüss  
232 Scientific) equipped with a microsyringe and CF03 high-speed camera with CMOS sensor. Water at  
233 different pH (pH 7 and 3) and medium-chain triglyceride (MCT) oil were tested on a disk of curcumin  
234 pressed powder. Disks of approximately 100 mg were prepared by placing gently ground powder  
235 between the plates of a hydraulic bench press with a diameter of 1.2 cm and pressing the sample

236 under a pressure of 200 bar for 30 seconds. Two trace paper disks were inserted between the plates  
237 to ensure the formation of a homogeneous and smooth disc surface. The measurements were  
238 conducted at room temperature. Water and oil droplets (2  $\mu\text{L}$  droplet volume) were placed onto the  
239 disk surface using a needle, and the droplet behavior was recorded with a camera. The droplet  
240 contour was analysed using the Young-Laplace method with Krüss Advance 1.12.0.35401 software,  
241 and the contact angle between the disk substrate and the water ( $\theta_1$ ) or oil droplet ( $\theta_2$ ) determined.  
242 Each measurement was performed five times to ensure accuracy. The three phase contact angle  
243 curcumin, oil and water ( $\theta_3$ ) was calculated from these two values using the following equations  
244 (referring to the schematic of Figure 2):

$$245 \quad \gamma_{CA} - \gamma_{CW} - \gamma_{AW} \cos \theta_1 = 0$$

$$246 \quad \gamma_{CA} - \gamma_{CO} - \gamma_{AO} \cos \theta_2 = 0$$

$$247 \quad \gamma_{CW} - \gamma_{CO} - \gamma_{WO} \cos \theta_3 = 0$$

248 where the  $\sigma$  values are the surface tensions among the different phases: air (A), curcumin (C) and  
249 water (W). Most of these values were taken from literature and are respectively:  $\gamma_{AO} =$   
250  $30.14 \text{ mN/m}$ ,  $\gamma_{AW} = 72.8 \text{ mN/m}$  and  $\gamma_{OW} = 24.77 \text{ mN/m}$ . Rearranging the three previous  
251 equations we can obtain the desired value  $\theta_3$ :

$$252 \quad \cos \theta_3 = \frac{\gamma_{AO} \cos \theta_2 - \gamma_{AW} \cos \theta_1}{\gamma_{WO}}$$

### 253 **1.7 Emulsions preparation and characterization**

254 **Preparation of W/O emulsions:** Water in oil (W/O) emulsions were prepared using the conditions  
255 shown in Table 3. The curcumin particle concentration was fixed, while the effect of different  
256 amounts of water, the pH and the speed of stirring was tested. Curcumin recrystallized particles were  
257 first dispersed in the continuous phase, MCT oil, using the Ultra-Turrax mixer, operating at 10000  
258 rpm for 3 minutes. Water was then added as the dispersed phase, at pH 7 and 3. Two different pH  
259 values, pH 3 and pH 7, were tested to appreciate differences in the interface stabilization of curcumin  
260 particles. The pH values were chosen to keep the product safe for human consumption. pH >7 was  
261 not considered as curcumin undergoes chemical degradation at basic environment (Priyadarsini,  
262 2009). The aqueous phase was mixed with the oil dispersion for 1 minute (experimental conditions  
263 in Table 2). After preparation, the emulsions were sealed with Parafilm and stored at room  
264 temperature in a dark place. For the preparation of the emulsions, both for W/O and O/W, curcumin

Commentato [ES1]: @Giulia: Inserire le references per i valori di tensioni interfacciale

265 crystals from experiments 13,14, 15 and 16 reported in *Table 1* were used. Although the  
266 characterization of the samples revealed no significant differences between the batches, the  
267 samples were selected because they were the most similar in terms of mean value of particle size,  
268 aspect ratio and morphology.

269 **Preparation of O/W emulsions:** Recrystallized curcumin powder was dispersed in the continuous  
270 phase (Milli-Q Water), followed by the addition of the dispersed phase (MCT oil), and the system  
271 was further mixed for several minutes. The pH of the acidic water was adjusted by adding a few  
272 drops of an aqueous solution of 0.1 M HCl. Different dispersing and emulsification methods, such as  
273 Ultra-Turrax mixing, ultrasound bath and handshaking, were tested, curcumin crystals load and  
274 amount of oil were evaluated, as reported in *Table 3*. The emulsions were sealed with Parafilm and  
275 stored at room temperature in a dark place.

276 **Characterization and stability assessment of curcumin emulsions:** Optical microscopy was  
277 used to measure the size distribution of the dispersed phase in the emulsions prepared with  
278 curcumin crystals. A Zeiss Axiolab 5 microscope at 5X and 10X magnifications was used for this  
279 purpose; images were collected with a digital camera with 48 Mp, resolution 4000 x 3000 pixels.  
280 The images collected were analysed using ImageJ version 1.52g, as described above for the crystal  
281 size distribution measurements with SEM. For each sample, the Feret diameter of 100 droplets  
282 minimum were considered.

283 To examine the structure of both water-in-oil (W/O) and oil-in-water (O/W) emulsion droplets, a  
284 spinning disk confocal microscope (Nikon Eclipse Ti-e fluorescence optical inverted microscope) was  
285 utilized, equipped with crest large FOV lasers and a super bright wide-spectrum source (Shutter  
286 Lambda XL), a high-resolution camera (Zyla 4.2 Plus, 4098 × 3264 pixels, Andor Technology), and a  
287 motorized stage. 10 µL of the sample was carefully placed onto a glass slide, ensuring the absence  
288 of any air gaps between the sample and the coverslip. The emulsions were gently agitated before  
289 the measurement to ensure homogeneity. Brightfield, green and red emission images, recorded with  
290 a light excitation of 488 nm and 550 nm, respectively, were acquired using a 20x objective (Nikon).  
291 In order to assess the stability against coalescence of the prepared emulsions, all samples were kept  
292 at room temperature and protected from light for several months. Samples were periodically  
293 checked visually to observed phase separation and with optical microscopy to quantify droplet size  
294 distribution.

295

296

## **2. . RESULTS & DISCUSSION**

297 **2.1 Curcumin crystals preparation and characterization**

298 Sub-micrometer curcumin crystals were successfully produced via anti-solvent crystallization. The  
299 chosen anti-solvent technique and the parameters tested aimed to maximize supersaturation  
300 conditions, promoting nucleation over growth (Meenan, 2001), and yielding small crystals with  
301 narrow size distribution. A high yield of recovery from the liquid, ranging from 80% to 94% w/w (ratio  
302 between starting material weight and recovered powder weight) was also favoured with this method  
303 (data in *Supporting Info, Table S3*). To define the crystallization parameters to test, in terms of solute  
304 concentration and solvent-antisolvent ratio, previous solubility measurements of curcumin in  
305 ethanol and in ethanol-water analytes with increasing water content were performed. *Figure 3 a*  
306 *and b* show respectively the solubility of raw curcumin in ethanol at different temperatures (ter Horst  
307 et al., 2009) and the solubility of curcumin in ethanol-water mixtures. Further information related  
308 to this data is shown in *Supporting Information Figure S2*. Upon resuspension in water of the  
309 obtained crystals, a fine, homogeneous, dispersion was formed, with a considerable improvement  
310 in ease of dispersion compared to the raw curcumin. To confirm the absence of chemical degradation  
311 or amorphization during particle formation and identify the crystal form, various analytical  
312 techniques, including Raman spectroscopy, powder X-ray diffraction (PXRD), Solid-State Nuclear  
313 Magnetic Resonance (SSNMR) and Differential Scanning Calorimetry (DSC) were used. The analyses  
314 were conducted on the recrystallized samples and the raw untreated material. The particle  
315 morphology and size distribution were evaluated through SEM imaging.

316 Various characterization techniques, including Raman spectroscopy, PXRD, SSNMR and DSC were  
317 performed on each crystallized sample to determine crystallinity, polymorphic form, and thermal  
318 properties. The polymorphic form of the crystals obtained via anti-solvent precipitation experiments  
319 was always the metastable form III of curcumin (Thorat & Dalvi, 2014). This metastable form  
320 formation is favoured by the high supersaturation achieved at high water to ethanol solution ratios  
321 (Coquerel, 2014; Roelands et al., 2006) and with the rapid mixing provided by the UltraTurrax. The  
322 crystallized material exhibited a characteristic red-orange colour compared to the yellow-orange of  
323 the raw curcumin (*Supporting Info, Figure S3*), which was found to be stable Form I of curcumin.

324 The formation of polymorph form III was confirmed by PXRD analysis and comparing the collected  
325 powder patterns to the calculated ones from crystallographic data from literature (*Figure 4*). The  
326 PXRD diffractograms show high crystallinity (e.g., sharp peaks) of the curcumin particles from anti-  
327 solvent precipitation, and homogeneity in terms of polymorphism. DSC thermograms of raw and  
328 recrystallized curcumin (form I and form III) are presented in *Figure 5*. Form I exhibits an endothermic  
329 peak at 178°C, corresponding to melting of the sample. In the thermogram of form III, the first peak  
330 at 161°C corresponds to an endothermic solid-state transformation to form I, as confirmed by other  
331 studies (Pandey & Dalvi, 2019; Thorat & Dalvi, 2015). The second endothermic peak at 179.5 °C  
332 corresponds to the melting of form I (Sanphui et al., 2011; Thorat & Dalvi, 2015). The slightly  
333 different onset of melting between the two samples can be attributed to the different particle sizes  
334 (Lee et al., 2001).

335 Due to the high similarity between the diffraction patterns of curcumin form II and III (Sanphui et al.,  
336 2011), SSNMR analysis was also performed to further confirm the polymorphic form of the anti-  
337 solvent curcumin crystals. This solid-state characterization technique allows discerning different  
338 crystalline forms with great accuracy due to its high sensitivity to the chemical surroundings of the  
339 nuclei constituting the system (Chierotti et al., 2010).

340 The most important structural difference between forms II and III is the number of independent  
341 molecules: one for the latter ( $Z = 8, Z' = 1$ ), as in form I, and two for form II ( $Z = 8, Z' = 2$ ), making  
342 them easily distinguishable by SSNMR (Dai et al., 2020). In fact,  $Z' = 2$  results in a splitting of all signals  
343 in the spectrum, except for some casual overlapping. *Figure 6* shows the  $^{13}\text{C}$  CPMAS SSNMR spectra  
344 of raw and recrystallized curcumin.

345 Only two signals can be observed for C2 and C2' (*Figure 1*). More than any others these signals allow  
346 a distinction between the different polymorphic forms: for raw curcumin they are found at 187.1  
347 and 182.6 ppm, while for recrystallized curcumin at 188.9 and 177.9 ppm. These results are in good  
348 agreement with what have been reported in the literature for form I and III, respectively (*Table 4*)  
349 (Dai et al., 2020), indicating that the raw curcumin mainly consists of curcumin form I, while the  
350 recrystallized one of form III. The presence of single signals for the two expected C atoms in this  
351 region definitively rules out the formation of form II, for which a number of signals of four, two for  
352 C2 and two for C2', is expected. However, spurious signals are observed in both  $^{13}\text{C}$  CPMAS spectra:  
353 at 184.9 ppm and at 158.8 ppm for raw curcumin and at 158.4 ppm for the recrystallized one. These  
354 impurities are likely due to the presence of curcumin derivatives, such as demethoxycurcumin and

355 bisdemethoxycurcumin (Siudem et al., 2023). As mentioned earlier, given the absence of  
356 involvement of curcumin methoxy groups in H-bonds or significant intramolecular interaction that  
357 can be responsible for molecular torsion, the presence of these derivatives does not affect greatly  
358 the properties of the compound.

359 Raman microscopy was used to obtain 2D maps of all the curcumin crystals obtained via anti-solvent  
360 precipitation to verify the homogeneity of the samples. *Figure 7* shows the Raman spectra of  
361 monoclinic form I and orthorhombic form III. The latter exhibits a unique peak at  $1532\text{ cm}^{-1}$ ,  
362 corresponding to intermolecular interactions in the central keto-enol region. Form I shows enhanced  
363  $\nu(\text{C}=\text{C})$  stretching vibrations. These two peaks were used to unequivocally identify the two forms  
364 (Prasad et al., 2020) in each collected map. All samples were found to be homogenous in terms of  
365 polymorphism, with only form III detected in all spectra collected for each map (example of  
366 measurement shown in *Supporting Info, Figure S3*).

367 As the recrystallized Form III is thermodynamic unstable at ambient conditions we checked for its  
368 kinetic stability (e.g., slow kinetic of polymorphic transformation) in air and water. In fact, a  
369 kinetically stable solid can still be used for Pickering formulations. Form III samples did not show  
370 polymorphic changes when stored at room conditions in a dark place for over 10 months. In situ  
371 Raman was used to check kinetic stability of Form III in water slurry; *Figure 8* shows that no  
372 significant differences in Raman spectra were observed over the 63 hr of the experiment, indicating  
373 the absence of phase transformation or degradation of curcumin crystals. Slurries of curcumin in  
374 water were further check after 3 months and show the persistence of Form III. Therefore, it can be  
375 concluded that form III has reasonable kinetic stability and may be used in Pickering formulations  
376 with long shelf-life .

377 SEM images of recrystallized curcumin particles obtained from one batch (Exp 1 reported in *Table 1*)  
378 are reported in *Figure 9*. Crystals show fairly narrow size and shape distributions, predominantly  
379 exhibiting a needle/rod-like shape (*Figure 9a-b*). Additionally, aggregates of crystals can be observed,  
380 potentially formed during filtration. Furthermore, dendritic structures (*Figure 9c-d*) can be observed,  
381 likely formed due to secondary nucleation, which is influenced by the mixing conditions and the level  
382 of supersaturation used during the experiments. The high-speed rotor-stator mixing employed in  
383 this study generates shear forces and turbulent flow, facilitating mixing and mass transfer but also  
384 leading to crystal breakage or aggregation (*Figure 9c-d*). Fragile crystals that grew as dendrites or  
385 needles were more prone to breakage into smaller particles.

386 Quantification of morphology (aspect ratio) and size distributions of crystallized curcumin particles  
387 were determined by examining SEM images at various magnifications for all 25 samples. The results  
388 for a representative experiment are graphically shown in *Figure 10 (Exp 1 of Table 1)*; whereas the  
389 average size and aspect ratio values with their standard deviation are reported in Supporting  
390 Information Table S3. The crystallized samples exhibited a narrow distribution of equivalent  
391 diameters, ranging from 0.5 to 1.2  $\mu\text{m}$ , with a mean aspect ratio ranging from 1.6 to 3.5. Supporting  
392 Information *Figure S4* shows the results of the statistical analysis performed on the size and shape  
393 average values; this analysis demonstrates that there is no significant relationship between  
394 operating parameters (e.g., stirring rate, volume ratio) explored and the resulting particle size and  
395 morphology, within the chosen design space. This might be related to the fact that similar, high levels  
396 of curcumin supersaturations were used in all experiments, despite changes in solvent to antisolvent  
397 ratios and curcumin initial concentrations. At such high levels of supersaturations, it is possible that  
398 the effect of other operating conditions on crystal size and shape distributions might be negligible.

399 A noticeable reduction in particle size was observed when comparing the shape and size of the  
400 curcumin crystallized via anti-solvent with the raw material provided by the supplier (mean  
401 equivalent diameter of 3.8  $\mu\text{m}$  and mean aspect ratio of 1.4). Additionally, the higher average aspect  
402 ratio in the recrystallized samples indicated a more acicular shape compared of anti-solvent  
403 crystallized curcumin compared to the raw material.

404 The interfacial behaviour of curcumin particles (raw and from anti-solvent crystallization) was  
405 determined through contact angle measurements ( $\theta_1$  and  $\theta_2$ ), which are reported in Table 6.  
406 Curcumin raw powder (form I) showed a hydrophobic nature with a value of  $\theta_1$  of around  $90^\circ$ , and  
407 more affinity with the oil phase ( $\theta_2$  around  $29^\circ$ ). The recrystallized form III has similar affinity to oil  
408 ( $\theta_2$  is about  $24^\circ$ ) but shows a more hydrophilic nature with an average value of  $\theta_1$  of  $62.4^\circ$ . Non-  
409 significant differences in values of  $\theta_1$  were observed with water at different values of pH. The values  
410 of measured contact angle explain the better dispersibility of the recrystallized Form III in water,  
411 compared with the raw Form I material. The minimum calculated  $\theta_3$  value (considering the  
412 measurement standard deviation) for Form I at pH=7 is around  $36^\circ$ , which indicates suitability for  
413 water in oil emulsion stabilization. The  $\theta_3$  value for the recrystallized curcumin ranges from 81 to  
414  $124^\circ$ , which indicates the potential of curcumin particles for stabilization of both O/W and W/O  
415 emulsions. It is worth noticing the considerably higher standard deviation of the measurements  
416 conducted on Form III in water compared to Form I. This might be related to the smaller size of the

417 recrystallized particles, which significantly affected the quality of the compressed disk (e.g., higher  
418 surface roughness, difficulties in powder handling). Despite the larger standard deviation, the higher  
419 hydrophilicity of form III is evident. This is likely related to the different molecular termination  
420 characterizing the facets of the two curcumin polymorphs. In fact, different polymorphs of the same  
421 compound can expose different functional groups of their constituting molecules on their facets,  
422 affecting facet-specific surface properties. Additionally, it has been reported that polymorphs usually  
423 differ in surface roughness (Montis et al., 2020), which can also affect wettability. To verify this  
424 hypothesis a computational study of the two crystal structures was performed using Mercury and  
425 Materials Studio. Figure 11 shows the predicted morphology of curcumin form I and form III (Figure  
426 11 a and b) and a graphical representation of the topology for the largest facets identified (Figure 11  
427 c and d). As visible from Table 5, both the polymorphs show a high contribution of the van der Waals  
428 interactions (i.e.  $\pi$ - $\pi$  stacking) for all the crystal facets. The contribution of the hydrogen bond and  
429 electrostatic interactions to the total lattice energy is minimal for Form I. Indeed, as shown in Figure  
430 11 a, neither of the facets' termination show any hydrogen bond acceptor or donor groups (e.g.  
431 methoxy and hydroxy groups). On the other hand, curcumin form III shows a slightly higher  
432 contribution of both hydrogen bond and electrostatic interactions to the total lattice energy; this is  
433 demonstrated by the presence of hydrogen acceptor and donor groups on the most of Form III facets  
434 (Figure 11 b). Comparing the two topologies (Figure 11 c and d) form III presents a higher surface  
435 roughness compared to Form I (more details are given in Supporting Info Figure S6 and Figure S7).  
436 The computational analysis is, therefore, in agreement with the experimental data that indicates a  
437 more hydrophilic nature of curcumin form III compared to form I.

#### 438 2.4 Emulsions preparation and characterization

439 Water-in-oil (W/O) emulsions were prepared using the conditions reported in Table 3. Figure 12  
440 shows the visual appearance of the prepared emulsions, which did not show evident phase  
441 separation for solid particles and the two liquid phases. It is worth noticing that water droplet  
442 sedimentation was observed within a few minutes of preparation of the W/O emulsions due to the  
443 large average size the dispersed phase. Confocal fluorescence microscopy of the samples was  
444 performed to check the type of the formed emulsion and to assess the interfacial activity of  
445 curcumin particles. Figure 13 clearly shows that a Pickering stabilized W/O emulsion is formed; water

446 droplets are surrounded by curcumin particles adsorbed at the water/oil interface. The yellow color  
447 is due to the colocalization of curcumin emitting both in the green channel, when dissolved in MCT  
448 oil, and in the red channel as solid phase. It is worth noticing that neither MCT oil nor water were  
449 stained with other dyes, hence the natural green fluorescence is due to dissolved curcumin.). The  
450 arrangement of curcumin particles around the water droplets indicates the typical droplet bridging  
451 of Pickering emulsions (French et al., 2015), which provides improved stability to the droplets and  
452 reduces coalescence over time.

453 The size distribution of water droplets in each emulsion sample was measured via optical light  
454 microscopy. All droplet size distributions are reported in Figure 14; whereas the average values with  
455 corresponding standard deviations are reported in Table 7. Water droplets were found to be  
456 between 70 to around 100  $\mu\text{m}$  in equivalent diameter, which is consistent with the mean size of the  
457 curcumin particles used. It can be observed that higher contents of water in the emulsions  
458 determined higher average droplet sizes and improved interfacial coverage by particles (as shown  
459 more clearly in Figure 15 m-n-o-p). In general, all droplet size distributions are quite broad, as shown  
460 by the relatively large standard deviations ranging from 30 to over 100  $\mu\text{m}$ . Increasingly broader  
461 droplet size distribution can be observed as the amount of dispersed phase in the emulsions  
462 increases, as clearly shown in Figure 14 a to c. Nevertheless, the presence of these smaller droplets  
463 is beneficial, as they form a particle/droplet network that provides bulk stabilization to the emulsions  
464 via a bridging mechanism (as shown more in details in Supporting Info, Figure S8).

465 The type of stirring had a weak effect on the average size and standard deviation of the droplet  
466 distributions; slightly larger and broader distributions were observed with handshaking compared  
467 to high-shear mixing (e.g., Emu W/O 1 vs 2, 4 vs 5 and 10 vs 11). However, in Figure 15 it can be  
468 observed that an increase in shear resulted in a higher occurrence of droplet bridging, in agreement  
469 with previous studies reported by French et al. (French et al., 2015). Additionally, higher shear led to  
470 the more uniform surface coverage from the particles and fewer solid particles dispersed in the

Commentato [ES2]: @Giulia: inserire references

471 continuous oil phase. These observations are shown more clearly in Figure 15 a to l). The pH of the  
472 water phase also influenced the emulsion microstructure. By comparing Emu W/O 1 and 4, and 7  
473 and 10 (Figure 14 and Table 7) it is possible to observe the effect of pH on droplet size distribution.  
474 Emulsions prepared with lower pH exhibited larger droplets compared to those prepared at pH 7,  
475 which is consistent with previous findings of Luo et al. evaluating the efficiency of flavonoids as  
476 stabilizers in biphasic systems (Luo et al., 2011).

477 A decrease in pH led to the formation of large aggregates of curcumin particles (Figures 13 e-f-j-k,  
478 opaque spots), which reduced the number of available particles for interfacial stabilization.

479 Despite the relatively large droplet sizes, the W/O emulsions prepared with curcumin particles did  
480 not show significant visual changes over several weeks of storage. A representative example of long-  
481 term stability is shown in Figure 16, which depicts the appearance of the Emu W/O 16 emulsion four  
482 months after preparation.

483 A further demonstration of the interfacial adsorption of curcumin particle in W/O emulsions is  
484 shown in Figure 17, which shows sample Emu W/O 16 left on a glass for 30 min. The deflated shape  
485 of the partially dried water droplets is due to the presence of Pickering particles (Okada et al., 2012),  
486 which are strongly adsorbed at the interface and prevent further water diffusion and evaporation by  
487 reducing the surface available for mass transfer.

488 Since  $\theta_3$  of recrystallized curcumin particles from anti-solvent precipitation was found to be in a  
489 range that indicated potential for O/W stabilization, this type of emulsions were also tested.  
490 Emulsions were prepared by dispersing recrystallized curcumin particles at different wt % contents,  
491 varying the MCT oil wt%, and testing different stirring techniques, as reported in Table 2. As shown  
492 in Figure 18 the resulting emulsions were unstable, leading to droplet coalescence, phase separation  
493 and particle precipitation within a few hours regardless of the different parameters tested. Visual  
494 inspection of the vials revealed large droplet sizes (Figure 18-a), regardless of the method of  
495 preparation and the composition. It is evident that the produced curcumin particles are not suitable  
496 for O/W stabilization; indeed a phase inversion was observed in the produced samples

497 (Binks, 2002). Figure 19 shows confocal fluorescence microscope images of the orange, superficial  
498 layer visible in the vials of Figure 18a: large oil domains (in green) containing smaller water droplets  
499 surrounded by curcumin particles (in yellow at O/W interfaces) are clearly visible. Even though  
500 contact angle measurements showed no significant differences in wettability between water at

501 different pHs, in sample Emu W/O 5.2 (*Figure 18 -b*) where water at pH 3 was used, the preference  
502 for curcumin particles to stay in the oil phase was more evident, with all the oil and curcumin  
503 particles moving on the top layer. Moreover, no particle precipitation was observed in the water  
504 phase when acidic water was used.

505

### 506 **3. Conclusions**

507 Crystallization techniques that enable consistent control over particle properties such as size, shape,  
508 and polymorphism are essential to produced Pickering formulation with tailored properties for many  
509 applications in the food sector. In this study, we applied crystal engineering tools and good practise  
510 to develop a robust anti-solvent crystallization method to produce submicron-sized curcumin  
511 crystals of suitable for Pickering stabilization. The process developed delivered curcumin particles  
512 with a uniform average size (0.5 - 1.2  $\mu\text{m}$ ), morphology (rodlike shape), and polymorphic form (the  
513 metastable form III). The curcumin particles recrystallized via anti-solvent exhibited improved  
514 dispersibility in water and enhanced hydrophilicity compared to the raw material as purchased  
515 (stable form I). This is due to the reduced size of the crystallized particles and the facet-specific  
516 surface chemistry of curcumin form III, as shown by computational modelling of the two polymorph  
517 structures.

518 Various conditions were investigated in the formulation of O/W and W/O Pickering emulsions,  
519 including the water to oil ratio, the type of emulsification technique, and the pH of the water phase.  
520 Consistent with the findings of previous studies conducted by Zembyla et al. (Zembyla et al., 2018,  
521 2019), it was observed that curcumin particles provided superior stabilization of W/O emulsions  
522 compared to O/W ones. Indeed the O/W samples produced in this work were highly unstable and  
523 even show phase inversion. As expected, larger water droplets were observed at higher ratios of  
524 water to oil in emulsion, with better particle coverage and bridging phenomenon that provided  
525 further bulk stabilization. An increase in the stirring energy provided for emulsification, from  
526 handshaking to Ultraturrax mixing, resulted in slightly smaller droplet size. An acidic pH determined  
527 droplet enlargement and the formation of large particle aggregates that precipitated; this is probably  
528 due to the effect of solution ions on the surface charge of curcumin particles, which can increase  
529 particle-particle interactions rather than particle-interface interactions. Despite the formation of  
530 relatively coarse emulsions (average droplet diameter up to over 100 $\mu\text{m}$ ), the particles remained  
531 adsorbed at the W/O interface, with no phase separation was observed even after 4 months of

532 storage. These findings provide a deeper understanding on how crystalline properties, particularly  
533 polymorphism, can affect the effectiveness of Pickering particles. The relationship between crystal  
534 structure and facet-specific surface chemistry and topology can be predicted with crystal  
535 engineering modelling tools; whereas specific crystallization processes can be designed to precisely  
536 deliver the desired particle properties. The work presented here is a first example of the application  
537 of a crystal engineering approach to rational design of Pickering particles and formulations.

538

### 539 **Supporting information**

540 Further details on Design of Experiment (DoE) and responses analysis, particle size distribution  
541 determination, HPLC calibration curve of curcumin ethanolic solution, curcumin crystal simulated  
542 facet topology and water-in-oil emulsion details.

543

### 544 **Acknowledgments**

545 This project has received funding from the European Research Council (ERC) under the  
546 European Union's Horizon 2020 research and innovation programme (grant agreement No 949229,  
547 CryForm). The authors thank the Cambridge Crystallographic Data Centre for providing the Mercury  
548 license. The authors wish to express their appreciation to Janine Andrea Preston, Cecilia Fiore and  
549 Pierfrancesco Latorre for their expertise and assistance throughout all aspects of our study. Professor  
550 Antonio Buffo is acknowledged for useful discussion on surface tension and three phase contact  
551 angles.

552

553

554 **References**

- 555 Aditya, N. P., Hamilton, I. E., & Norton, I. T. (2017). Amorphous nano-curcumin stabilized oil in water  
556 emulsion: Physico chemical characterization. *Food Chemistry*, 224, 191–200.  
557 <https://doi.org/10.1016/j.foodchem.2016.12.082>
- 558 Albert, C., Beladjine, M., Tsapis, N., Fattal, E., Agnely, F., & Huang, N. (2019). Pickering emulsions:  
559 Preparation processes, key parameters governing their properties and potential for pharmaceutical  
560 applications. *Journal of Controlled Release*, 309, 302–332.  
561 <https://doi.org/10.1016/j.jconrel.2019.07.003>
- 562 Aveyard, R., Binks, B. P., & Clint, J. H. (2003). Emulsions stabilised solely by colloidal particles. *Advances in*  
563 *Colloid and Interface Science*, 100–102, 503–546. [https://doi.org/10.1016/S0001-8686\(02\)00069-6](https://doi.org/10.1016/S0001-8686(02)00069-6)
- 564 Binks, B. P. (2002). Particles as surfactants – similarities and differences. *Interface Science*.
- 565 Binks, B. P., & Lumsdon, S. O. (2000). Influence of Particle Wettability on the Type and Stability of Surfactant-  
566 Free Emulsions. *Langmuir*, 16(23), 8622–8631. <https://doi.org/10.1021/la000189s>
- 567 Chen, L., Ao, F., Ge, X., & Shen, W. (2020). Food-Grade Pickering Emulsions: Preparation, Stabilization and  
568 Applications. *Molecules*, 25(14), 3202. <https://doi.org/10.3390/molecules25143202>
- 569 Chevalier, Y., & Bolzinger, M.-A. (2013). Emulsions stabilized with solid nanoparticles: Pickering emulsions.  
570 *Colloids and Surfaces A: Physicochemical and Engineering Aspects*, 439, 23–34.  
571 <https://doi.org/10.1016/j.colsurfa.2013.02.054>
- 572 Chierotti, M. R., Ferrero, L., Garino, N., Gobetto, R., Pellegrino, L., Braga, D., Grepioni, F., & Maini, L. (2010).  
573 The Richest Collection of Tautomeric Polymorphs: The Case of 2-Thiobarbituric Acid. *Chemistry – A*  
574 *European Journal*, 16(14), 4347–4358. <https://doi.org/10.1002/chem.200902485>
- 575 Coquerel, G. (2014). Crystallization of molecular systems from solution: Phase diagrams, supersaturation  
576 and other basic concepts. *Chem. Soc. Rev.*, 43(7), 2286–2300. <https://doi.org/10.1039/C3CS60359H>
- 577 Dai, Y., Terskikh, V., Brinckmann, A., & Wu, G. (2020). Solid-State <sup>1</sup>H, <sup>13</sup>C, and <sup>17</sup>O NMR Characterization of  
578 the Two Uncommon Polymorphs of Curcumin. *Crystal Growth & Design*, 20(11), 7484–7491.  
579 <https://doi.org/10.1021/acs.cgd.0c01164>

580 Desiraju, G. R. (2013). Crystal Engineering: From Molecule to Crystal. *Journal of the American Chemical*  
581 *Society*, 135(27), 9952–9967. <https://doi.org/10.1021/ja403264c>

582 Dickinson, E. (2010). Food emulsions and foams: Stabilization by particles. *Current Opinion in Colloid &*  
583 *Interface Science*, 15(1–2), 40–49. <https://doi.org/10.1016/j.cocis.2009.11.001>

584 Ewens, H., Metilli, L., & Simone, E. (2021). Analysis of the effect of recent reformulation strategies on the  
585 crystallization behaviour of cocoa butter and the structural properties of chocolate. *Current*  
586 *Research in Food Science*, 4, 105–114. <https://doi.org/10.1016/j.crfs.2021.02.009>

587 Fang, L., Gao, Z., Gao, Z., Huang, W., Wan, X., Rohani, S., & Gong, J. (2023). Controlled crystallization of  
588 metastable polymorphic pharmaceutical: Comparative study of batchwise and continuous tubular  
589 crystallizers. *Chemical Engineering Science*, 266, 118277. <https://doi.org/10.1016/j.ces.2022.118277>

590 Frelichowska, J., Bolzinger, M.-A., Pelletier, J., Valour, J.-P., & Chevalier, Y. (2009). Topical delivery of lipophilic  
591 drugs from o/w Pickering emulsions. *International Journal of Pharmaceutics*, 371(1–2), 56–63.  
592 <https://doi.org/10.1016/j.ijpharm.2008.12.017>

593 French, D. J., Taylor, P., Fowler, J., & Clegg, P. S. (2015). Making and breaking bridges in a Pickering emulsion.  
594 *Journal of Colloid and Interface Science*, 441, 30–38. <https://doi.org/10.1016/j.jcis.2014.11.032>

595 Jafari, S. M., Sedaghat Doost, A., Nikbakht Nasrabadi, M., Boostani, S., & Van der Meeren, P. (2020).  
596 Phytoparticles for the stabilization of Pickering emulsions in the formulation of novel food colloidal  
597 dispersions. *Trends in Food Science & Technology*, 98, 117–128.  
598 <https://doi.org/10.1016/j.tifs.2020.02.008>

599 Klitou, P., Parisi, E., Bordignon, S., Bravetti, F., Rosbottom, I., Dell'Aera, M., Cuocci, C., Chierotti, M. R.,  
600 Altomare, A., & Simone, E. (2023). Navigating the Complex Solid Form Landscape of the Quercetin  
601 Flavonoid Molecule. *Crystal Growth & Design*, 23(8), 6034–6045.  
602 <https://doi.org/10.1021/acs.cgd.3c00584>

603 Klitou, P., Rosbottom, I., Karde, V., Heng, J. Y. Y., & Simone, E. (2022). Relating Crystal Structure to Surface  
604 Properties: A Study on Quercetin Solid Forms. *Crystal Growth & Design*, 22(10), 6103–6113.  
605 <https://doi.org/10.1021/acs.cgd.2c00707>

606 Leardi, R. (2009). Experimental design in chemistry: A tutorial. *Analytica Chimica Acta*, 652(1–2), 161–172.  
607 <https://doi.org/10.1016/j.aca.2009.06.015>

608 Lee, J.-S., Hsu, C.-K., & Jaw, K.-S. (2001). The thermal properties of KClO<sub>4</sub> with different particle size.  
609 *Thermochimica Acta*, 367–368, 381–385. [https://doi.org/10.1016/S0040-6031\(00\)00691-2](https://doi.org/10.1016/S0040-6031(00)00691-2)

610 Liu, Y., Niu, S., Lai, W., Yu, T., Ma, Y., Gao, H., Zhao, F., & Ge, Z. (2019). Crystal morphology prediction of  
611 energetic materials grown from solution: Insights into the accurate calculation of attachment  
612 energies. *CrystEngComm*, 21(33), 4910–4917. <https://doi.org/10.1039/C9CE00848A>

613 Luo, Z., Murray, B. S., Yusoff, A., Morgan, M. R. A., Povey, M. J. W., & Day, A. J. (2011). Particle-Stabilizing  
614 Effects of Flavonoids at the Oil–Water Interface. *Journal of Agricultural and Food Chemistry*, 59(6),  
615 2636–2645. <https://doi.org/10.1021/jf1041855>

616 Macrae, C. F., Bruno, I. J., Chisholm, J. A., Edgington, P. R., McCabe, P., Pidcock, E., Rodriguez-Monge, L.,  
617 Taylor, R., Streek, J. V. D., & Wood, P. A. (2008). Mercury CSD 2.0—New features for the visualization  
618 and investigation of crystal structures. *Journal of Applied Crystallography*, 41(2), 466–470.  
619 <https://doi.org/10.1107/S0021889807067908>

620 Meenan, P. (2001). From Molecules to Crystallizers An Introduction to Crystallization Roger Davey and John  
621 Garside. Oxford University Press, New York. 2000. ISBN 0198504896. *Crystal Growth & Design*, 1(1),  
622 101–101. <https://doi.org/10.1021/cg000012w>

623 Metilli, L., Storm, M., Marathe, S., Lazidis, A., Marty-Terrade, S., & Simone, E. (2022). Application of X-ray  
624 Microcomputed Tomography for the Static and Dynamic Characterization of the Microstructure of  
625 Oleofoams. *Langmuir*, 38(4), 1638–1650. <https://doi.org/10.1021/acs.langmuir.1c03318>

626 Nelson, K. M., Dahlin, J. L., Bisson, J., Graham, J., Pauli, G. F., & Walters, M. A. (2017). The Essential  
627 Medicinal Chemistry of Curcumin: Miniperspective. *Journal of Medicinal Chemistry*, 60(5), 1620–  
628 1637. <https://doi.org/10.1021/acs.jmedchem.6b00975>

629 Pandey, K. U., & Dalvi, S. V. (2019). Understanding stability relationships among three curcumin polymorphs.  
630 *Advanced Powder Technology*, 30(2), 266–276. <https://doi.org/10.1016/j.apr.2018.11.002>

631 Peram, M. R., Jalalpure, S. S., Joshi, S. A., Palkar, M. B., & Diwan, P. V. (2017). Single robust RP-HPLC  
632 analytical method for quantification of curcuminoids in commercial turmeric products, Ayurvedic  
633 medicines, and nanovesicular systems. *Journal of Liquid Chromatography & Related Technologies*,  
634 40(10), 487–498. <https://doi.org/10.1080/10826076.2017.1329742>

635 Prandini, E., Cali, E., Maloney, A. G. P., Parisi, E., & Simone, E. (2024). Predicting particle quality attributes of  
636 organic crystalline materials using Particle Informatics. *Powder Technology*, 443, 119927.  
637 <https://doi.org/10.1016/j.powtec.2024.119927>

638 Prasad, R., Gupta, K. M., Poornachary, S. K., & Dalvi, S. V. (2020). Elucidating the Polymorphic Behavior of  
639 Curcumin during Antisolvent Crystallization: Insights from Raman Spectroscopy and Molecular  
640 Modeling. *Crystal Growth & Design*, 20(9), 6008–6023. <https://doi.org/10.1021/acs.cgd.0c00728>

641 Preston, J. A., Parisi, E., Murray, B., Tyler, A. I. I., & Simone, E. (2024). Elucidating the Polymorphism of  
642 Xanthone: A Crystallization and Characterization Study. *Crystal Growth & Design*, 24(8), 3256–3268.  
643 <https://doi.org/10.1021/acs.cgd.3c01506>

644 Priyadarsini, K. I. (2009). Photophysics, photochemistry and photobiology of curcumin: Studies from organic  
645 solutions, bio-mimetics and living cells. *Journal of Photochemistry and Photobiology C:*  
646 *Photochemistry Reviews*, 10(2), 81–95. <https://doi.org/10.1016/j.jphotochemrev.2009.05.001>

647 Pugh, R. J. (2016). *Bubble and Foam Chemistry*. Cambridge University Press.  
648 <https://doi.org/10.1017/CBO9781316106938>

649 Roelands, C. P. M., Jiang, S., Kitamura, M., ter Horst, J. H., Kramer, H. J. M., & Jansens, P. J. (2006).  
650 Antisolvent Crystallization of the Polymorphs of L -Histidine as a Function of Supersaturation Ratio  
651 and of Solvent Composition. *Crystal Growth & Design*, 6(4), 955–963.  
652 <https://doi.org/10.1021/cg050529d>

653 Sanphui, P., & Bolla, G. (2018). Curcumin, a Biological Wonder Molecule: A Crystal Engineering Point of  
654 View. *Crystal Growth & Design*, 18(9), 5690–5711. <https://doi.org/10.1021/acs.cgd.8b00646>

655 Sanphui, P., Goud, N. R., Khandavilli, U. B. R., Bhanoth, S., & Nangia, A. (2011). New polymorphs of  
656 curcumin. *Chemical Communications*, 47(17), 5013. <https://doi.org/10.1039/c1cc10204d>

657 Sarkar, A., & Dickinson, E. (2020). Sustainable food-grade Pickering emulsions stabilized by plant-based  
658 particles. *Current Opinion in Colloid & Interface Science*, 49, 69–81.  
659 <https://doi.org/10.1016/j.cocis.2020.04.004>

660 Simone, E., & Nagy, Z. K. (2015). A link between the ATR-UV/Vis and Raman spectra of zwitterionic solutions  
661 and the polymorphic outcome in cooling crystallization. *CrystEngComm*, 17(34), 6538–6547.  
662 <https://doi.org/10.1039/C5CE00702J>

663 Simone, E., Zhang, W., & Nagy, Z. K. (2015). Application of Process Analytical Technology-Based Feedback  
664 Control Strategies To Improve Purity and Size Distribution in Biopharmaceutical Crystallization.  
665 *Crystal Growth & Design*, 15(6), 2908–2919. <https://doi.org/10.1021/acs.cgd.5b00337>

666 Siudem, P., Szeleszczuk, Ł., Zielińska, A., & Paradowska, K. (2023). 13C CPMAS NMR as an Alternative  
667 Method to Verify the Quality of Dietary Supplements Containing Curcumin. *Molecules*, 28(8), 3442.  
668 <https://doi.org/10.3390/molecules28083442>

669 Tan, C., & McClements, D. J. (2021). Application of Advanced Emulsion Technology in the Food Industry: A  
670 Review and Critical Evaluation. *Foods*, 10(4), 812. <https://doi.org/10.3390/foods10040812>

671 Tang, J., Quinlan, P. J., & Tam, K. C. (2015). Stimuli-responsive Pickering emulsions: Recent advances and  
672 potential applications. *Soft Matter*, 11(18), 3512–3529. <https://doi.org/10.1039/C5SM00247H>

673 ter Horst, J. H., Deij, M. A., & Cains, P. W. (2009). Discovering New Co-Crystals. *Crystal Growth & Design*,  
674 9(3), 1531–1537. <https://doi.org/10.1021/cg801200h>

675 Thorat, A. A., & Dalvi, S. V. (2014). Particle formation pathways and polymorphism of curcumin induced by  
676 ultrasound and additives during liquid antisolvent precipitation. *CrystEngComm*, 16(48), 11102–  
677 11114. <https://doi.org/10.1039/C4CE02021A>

678 Thorat, A. A., & Dalvi, S. V. (2015). Solid-State Phase Transformations and Storage Stability of Curcumin  
679 Polymorphs. *Crystal Growth & Design*, 15(4), 1757–1770. <https://doi.org/10.1021/cg501814q>

680 Wu, J., & Ma, G. (2016). Recent Studies of Pickering Emulsions: Particles Make the Difference. *Small*, 12(34),  
681 4633–4648. <https://doi.org/10.1002/smll.201600877>

682 Xia, T., Xue, C., & Wei, Z. (2021). Physicochemical characteristics, applications and research trends of edible  
683 Pickering emulsions. *Trends in Food Science & Technology*, *107*, 1–15.  
684 <https://doi.org/10.1016/j.tifs.2020.11.019>

685 Xiao, J., Sarker, S. D., & Asakawa, Y. (A c. Di). (2021). *Handbook of Dietary Phytochemicals*. Springer  
686 Singapore. <https://doi.org/10.1007/978-981-15-4148-3>

687 Yang, Y., Fang, Z., Chen, X., Zhang, W., Xie, Y., Chen, Y., Liu, Z., & Yuan, W. (2017). An Overview of Pickering  
688 Emulsions: Solid-Particle Materials, Classification, Morphology, and Applications. *Frontiers in*  
689 *Pharmacology*, *8*, 287. <https://doi.org/10.3389/fphar.2017.00287>

690 Zembyla, M., Murray, B. S., Radford, S. J., & Sarkar, A. (2019). Water-in-oil Pickering emulsions stabilized by  
691 an interfacial complex of water-insoluble polyphenol crystals and protein. *Journal of Colloid and*  
692 *Interface Science*, *548*, 88–99. <https://doi.org/10.1016/j.jcis.2019.04.010>

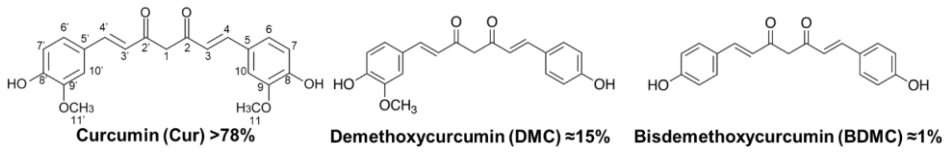
693 Zembyla, M., Murray, B. S., & Sarkar, A. (2018). Water-In-Oil Pickering Emulsions Stabilized by Water-  
694 Insoluble Polyphenol Crystals. *Langmuir*, *34*(34), 10001–10011.  
695 <https://doi.org/10.1021/acs.langmuir.8b01438>

696 Zembyla, M., Murray, B. S., & Sarkar, A. (2020). Water-in-oil emulsions stabilized by surfactants, biopolymers  
697 and/or particles: A review. *Trends in Food Science & Technology*, *104*, 49–59.  
698 <https://doi.org/10.1016/j.tifs.2020.07.028>

699  
700  
701  
702

703

704

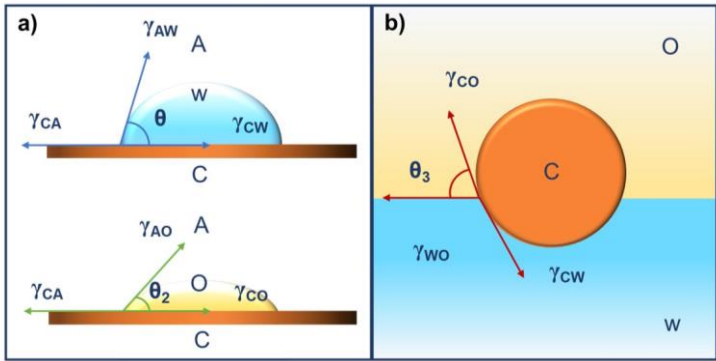


705

706 **Figure 1:** Curcuminoids molecular structure and relative amount of curcuminoids in the mixture. Atom  
707 numbering of the keto-enolic form of curcumin is reported.

708

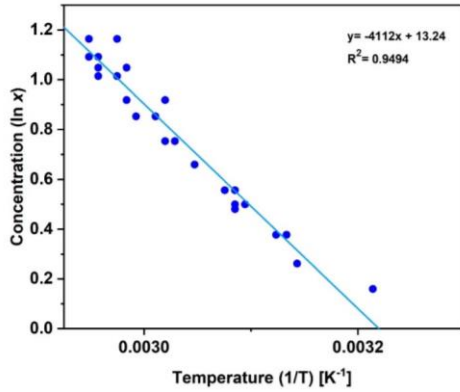
709



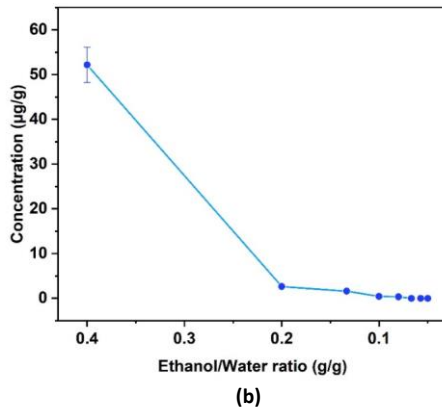
710  
 711  
 712  
 713  
 714

**Figure 2:** Schematic of surface tensions and contact angles for air, water and curcumin and air, oil and curcumin (a) and oil, water and curcumin (b)

715



716



717

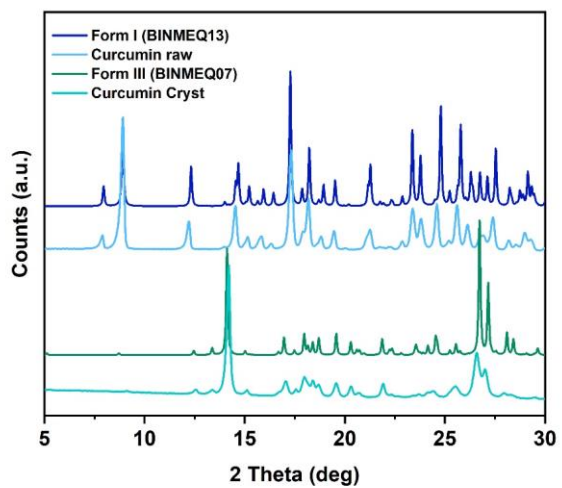
718 **Figure 3:** (a) Van't Hoff type plot of curcumin solubility in ethanol in the range 35-65 °C. In the y axis,  
719 concentration of curcumin as natural logarithm of the molar fraction (x), in the x axis the reciprocal of  
720 temperature in Kelvin. (b) Solubility curve of curcumin as a function of increasing water content. The amount  
721 of water increases from left to right.

722

723

724

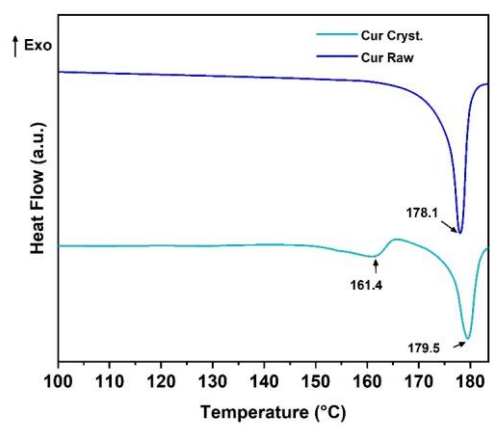
725



726

727 **Figure 4:** PXRD pattern of raw curcumin (on the top) and recrystallized curcumin (on the bottom). The  
728 experimental pattern) are compared with the simulated pattern obtained from CSD database.

729

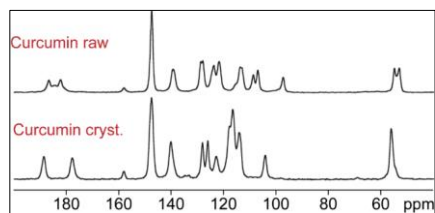


730

731 **Figure 5:** DSC thermogram of raw curcumin (on the top) and recrystallized curcumin (on the bottom).

732

733



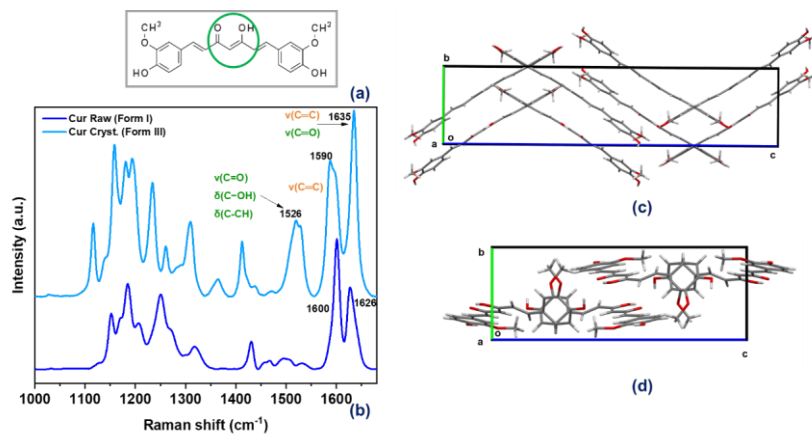
734

735 **Figure 6:** <sup>13</sup>C (100.63 MHz) CPMAS ssNMR spectra of the raw (top) and recrystallized curcumin (bottom)

736 *acquired at a spinning rate of 12 kHz.*

737

738



739

740 **Figure 7:** (a) Curcumin molecular structure. In green the region corresponding to keto-enol tautomerism is  
 741 highlighted. (b) Raman spectra of raw curcumin (on the bottom) and recrystallized curcumin (on the top),  
 742 corresponding to polymorphic form I and form III, respectively. (c) Crystal packing of orthorhombic curcumin  
 743 form III (BINMEQ07) and (d) monoclinic curcumin form I (BINMEQ13) along a axis.

744

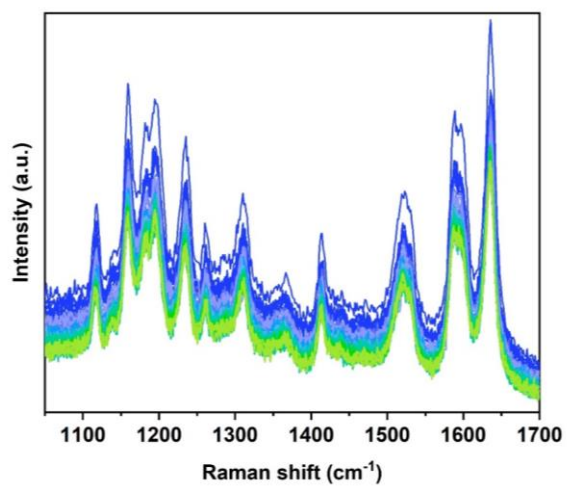
745

746

747

748

749

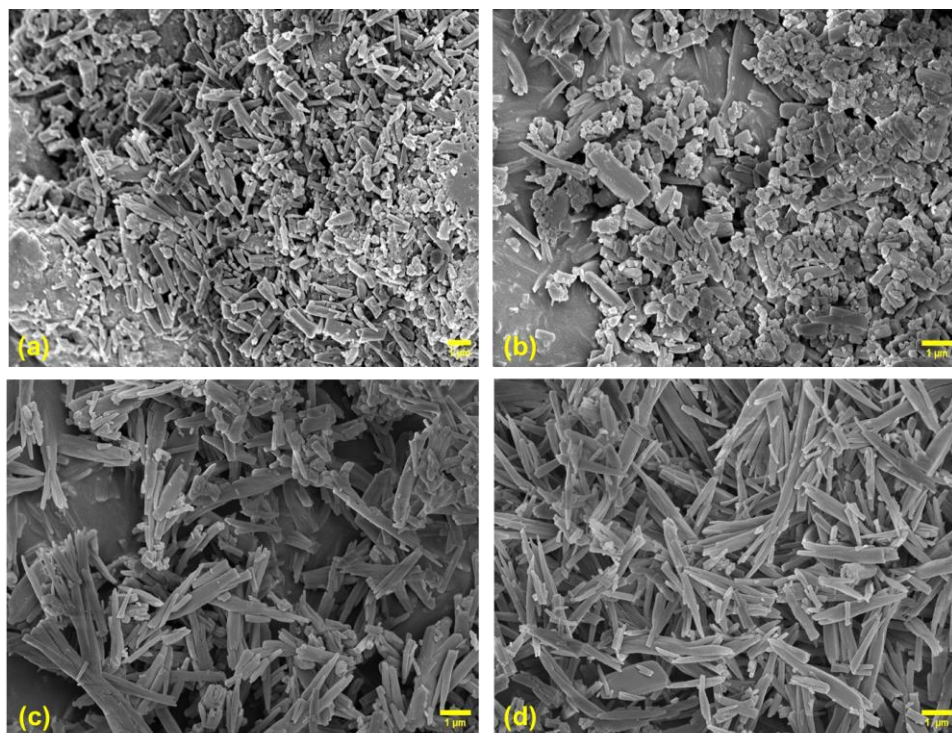


750

751 **Figure 8:** In situ Raman spectra of recrystallized curcumin slurry in water over time. The slurry was monitored  
752 for 63 hr, a total of 64 spectra were recorded

753

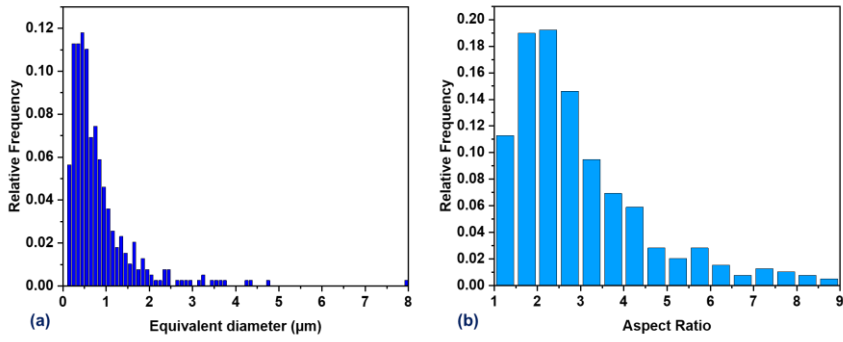
754  
755  
756



757

758 **Figure 9:** Recrystallized curcumin particles observed via SEM micrographs. Crystals were from Exp 1  
759 (conditions reported in Table 1). Images were obtained with a magnification of 20 000 X, except for image (a),  
760 obtained with 15 000 X magnification. Scale bars are reported for every micrograph. (a-b) show particles with  
761 a needle/rod-like morphology; (c-d) reveals the presence of dendritic, partly broken structures.

762



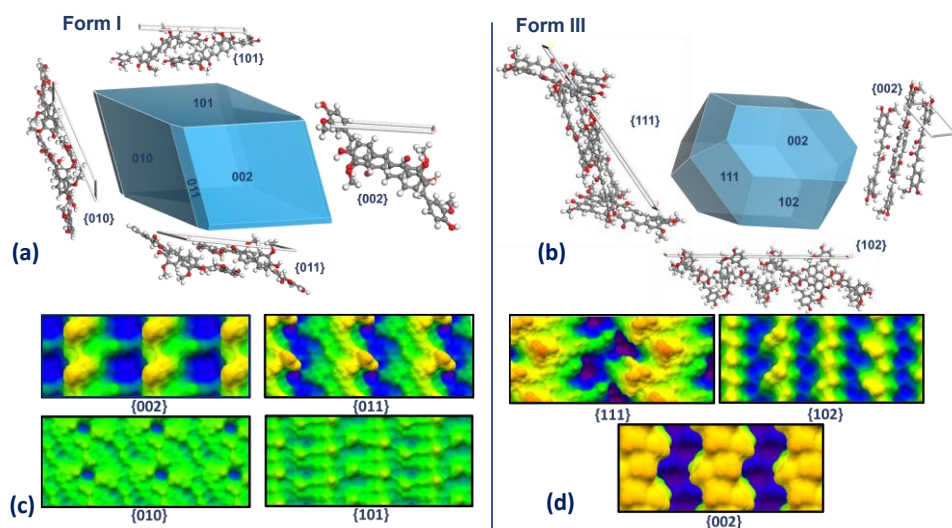
763

764 **Figure 10:** Particle size and morphology distributions of a recrystallized curcumin sample. (a) Equivalent  
 765 (Feret's) diameter and (b) aspect ratio of the particle population of Exp 1 (conditions reported in Table 1)  
 766 were considered.

767

768

769

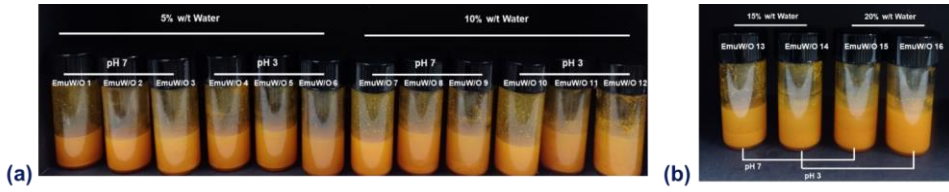


770

771 **Figure 11:** Morphology prediction and facet-specific topologies calculated using the attachment energy  
 772 model for curcumin form I (a) and form III (b). For the two morphologies, the topology of the most dominant  
 773 facets is reported. (c) and (d) show the surface analysis of the most dominant facets, expressed as the ratio  
 774 between effective and projected surface. Green regions are in line with the average plane considered by  
 775 calculations, while yellow/orange and blue/purple represent surfaces respectively above and below the  
 776 average plane.

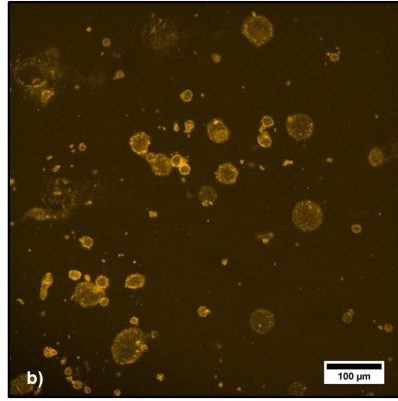
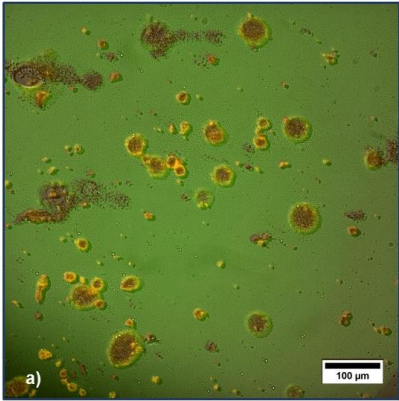
777

778  
779  
780



781  
782  
783  
784  
785

**Figure 12:** W/O emulsions prepared (a) varying the mixing condition and (b) fixing the speed of agitation at 10000 rpm. The load of curcumin particles was fixed.

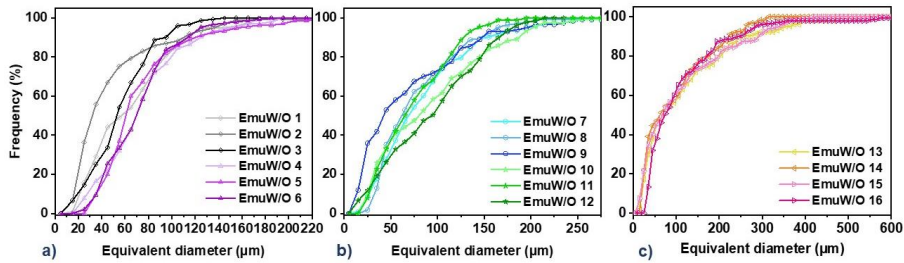


786

787 **Figure 13:** Confocal images of 20 wt% W/O emulsion stabilized by curcumin particles. (a) Merged channels  
788 of brightfield, green and red emission ones and (b) red channel images were collected for the same sample.  
789 The fluorescence of curcumin (both red as solid and green in MCT oil) causes the yellow colour at interfaces,  
790 whereas the green fluorescence is caused by partial dissolution of curcumin in the oil phase.

791

792



793

794 **Figure 14:** Emulsions droplet size distribution represented as cumulative frequency, expressed in percentage  
795 of droplet over the total number. The samples were grouped according to water content in W/O emulsions.  
796 In graph (a) emulsions prepared with 5 wt% of water can be observed, in (b) 10 wt% and (c) 15 to 20 wt%  
797 water contents are shown.

798

799

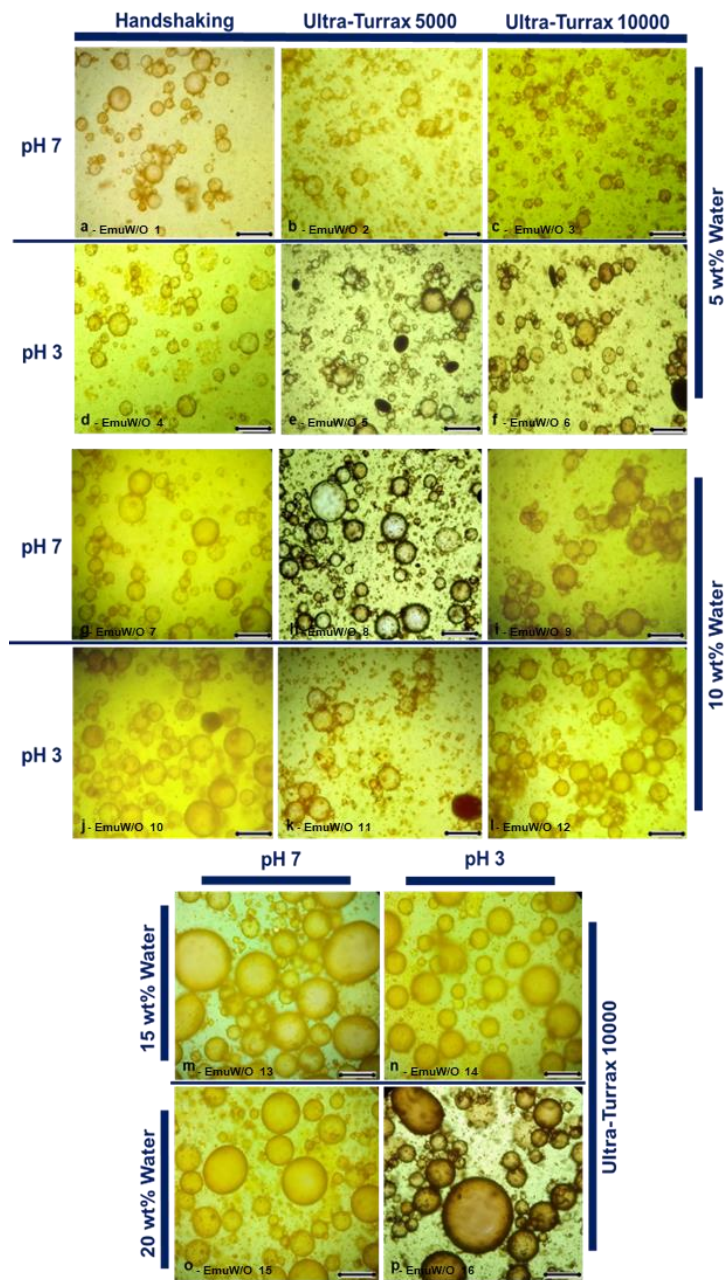
800

801

802

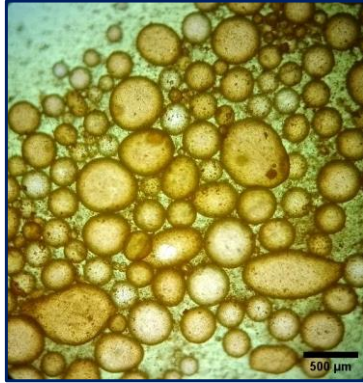
803

804



805

806 **Figure 15:** Images of W/O emulsion obtained through optical microscope. The scalebar is set to 250 μm for  
 807 all the samples.



808

809 **Figure 16:** *Emulsion Emu W/O 16 after 4 months of storage. Optical microscopy reveals an enlargement of*  
810 *the droplets and particle dispersed in the continuous phase.*

811

812

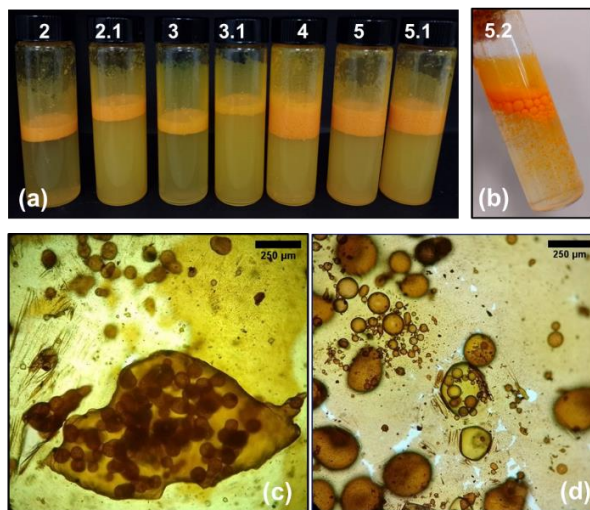


813

814 **Figure 17:** Sample Emu W/O 16 left in air on a glass slide for 30 minutes. The resulting deflated structure  
815 demonstrates that the particles are strongly adsorbed at the interface.

816

817

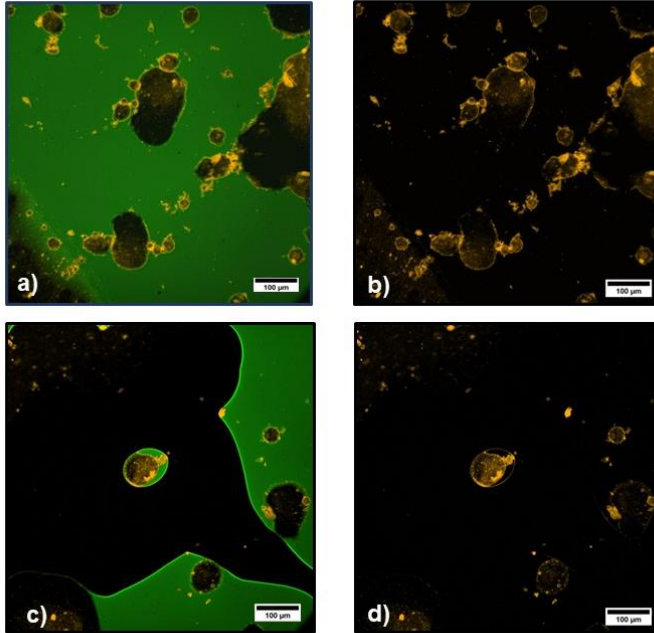


818

819 **Figure 18:** In O/W emulsions from 2 to 5.1 reported (a) water at pH 7 was used while (b) 5.2 sample was  
820 prepared with water at pH 3. Images obtained through optical microscope of sample 2 (c) and sample 5.1  
821 (d) are reported.

822

823



824

825 **Figure 19:** confocal images of sample Emu O/W 5. The auto-fluorescence of curcumin causes the yellow  
826 brightness. Green fluorescence is caused by partial dissolution of curcumin in the oil phase. Images (b) and  
827 (d) show curcumin only autofluorescence. Images a) and c) were obtained in brightfield option.

**Table 1:** List of the experiments performed. DoE approach was used. The four factors and the five levels were first combined in a full factorial design, for a total amount of 625 experimental points. ccdesign function was then applied to select the experiments from the experimental domain.

<b>Experiment #</b>	<b>Concentration (mg/g)</b>	<b>EtOH/Water Ratio</b>	<b>Water volume (ml)</b>	<b>Speed mixing (rpm)</b>
<b>Exp 1</b>	7.25	01:12.5	445	14900
<b>Exp 2</b>	7.25	01:12.5	445	18300
<b>Exp 3</b>	7.25	01:12.5	615	14900
<b>Exp 4</b>	7.25	01:12.5	615	18300
<b>Exp 5</b>	7.25	01:17.5	445	14900
<b>Exp 6</b>	7.25	01:17.5	445	18300
<b>Exp 7</b>	7.25	01:17.5	615	14900
<b>Exp 8</b>	7.25	01:17.5	615	18300
<b>Exp 9</b>	11.07	01:12.5	445	14900
<b>Exp 10</b>	11.07	01:12.5	445	18300
<b>Exp 11</b>	11.07	01:12.5	615	14900
<b>Exp 12</b>	11.07	01:12.5	615	18300
<b>Exp 13</b>	11.07	01:17.5	445	14900
<b>Exp 14</b>	11.07	01:17.5	445	18300
<b>Exp 15</b>	11.07	01:17.5	615	14900
<b>Exp 16</b>	11.07	01:17.5	615	18300
<b>Exp 17</b>	5.85	01:15	530	16600
<b>Exp 18</b>	13.58	01:15	530	16600
<b>Exp 19</b>	9.04	01:10	530	16600
<b>Exp 20</b>	9.04	01:20	530	16600
<b>Exp 21</b>	9.04	01:15	360	16600
<b>Exp 22</b>	9.04	01:15	700	16600
<b>Exp 23</b>	9.04	01:15	530	13200
<b>Exp 24</b>	9.04	01:15	530	20000
<b>Exp 25</b>	9.04	01:15	530	16600
<b>Exp 22</b>	9.04	01:15	700	16600
<b>Exp 23</b>	9.04	01:15	530	13200
<b>Exp 24</b>	9.04	01:15	530	20000
<b>Exp 25</b>	9.04	01:15	530	16600

**Table 2:** Experimental condition tested for the preparation of W/O emulsions

Experiment #	Oil (g)	Water (g)	pH	Curcumin (mg)	Mixing (rpm)
<b>Emu W/O 1</b>	4.73 (94.6 wt%)	0.25 (5 wt%)	7	20 (0.4 wt%)	Handshaking
<b>Emu W/O 2</b>	4.73 (94.6 wt%)	0.25 (5 wt%)	7	20 (0.4 wt%)	Ultra-Turrax 5000
<b>Emu W/O 3</b>	4.73 (94.6 wt%)	0.25 (5 wt%)	7	20 (0.4 wt%)	Ultra-Turrax 10000
<b>Emu W/O 4</b>	4.73 (94.6 wt%)	0.25 (5 wt%)	3	20 (0.4 wt%)	Handshaking
<b>Emu W/O 5</b>	4.73 (94.6 wt%)	0.25 (5 wt%)	3	20 (0.4 wt%)	Ultra-Turrax 5000
<b>Emu W/O 6</b>	4.73 (94.6 wt%)	0.25 (5 wt%)	3	20 (0.4 wt%)	Ultra-Turrax 10000
<b>Emu W/O 7</b>	4.48 (89.6 wt%)	0.5 (10 wt%)	7	20 (0.4 wt%)	Handshaking
<b>Emu W/O 8</b>	4.48 (89.6 wt%)	0.5 (10 wt%)	7	20 (0.4 wt%)	Ultra-Turrax 5000
<b>Emu W/O 9</b>	4.48 (89.6 wt%)	0.5 (10 wt%)	7	20 (0.4 wt%)	Ultra-Turrax 10000
<b>Emu W/O 10</b>	4.48 (89.6 wt%)	0.5 (10 wt%)	3	20 (0.4 wt%)	Handshaking
<b>Emu W/O 11</b>	4.48 (89.6 wt%)	0.5 (10 wt%)	3	20 (0.4 wt%)	Ultra-Turrax 5000
<b>Emu W/O 12</b>	4.48 (89.6 wt%)	0.5 (10 wt%)	3	20 (0.4 wt%)	Ultra-Turrax 10000
<b>Emu W/O 13</b>	4.23 (84.6 wt%)	0.75 (15 wt%)	7	20 (0.4 wt%)	Ultra-Turrax 10000
<b>Emu W/O 14</b>	4.23 (84.6 wt%)	0.75 (15 wt%)	3	20 (0.4 wt%)	Ultra-Turrax 10000
<b>Emu W/O 15</b>	3.98 (79.6 wt%)	1 (20 wt%)	7	20 (0.4 wt%)	Ultra-Turrax 10000
<b>Emu W/O 16</b>	3.98 (79.6 wt%)	1 (20 wt%)	3	20 (0.4 wt%)	Ultra-Turrax 10000

834

**Table 3:** Experimental condition tested for O/W emulsions

Experiment #	Oil (g)	Water (g)	Curcumin (mg)	Mixing (rpm)	
				Dispersion	Emulsification
<b>Emu O/W 2</b>	0.63 (5.2 wt%)	11.53 (94.7 wt%)	12.5 (0.1 wt%)	Ultra-turrax 10000 (3 min)	Ultra-turrax 10000 (1min)
<b>Emu O/W 2.1</b>	0.75 (5.2 wt%)	14.25 (94.7 wt%)	15 (0.1 wt%)	Ultra-turrax 4000 (5 min)	Ultrasound bath (2 min 40kHz) + Handshaking (1 min)
<b>Emu O/W 3</b>	0.63 (5.2 wt%)	11.53 (94.7 wt%)	6.25 (0.05 wt%)	Ultra-turrax 10000 (3 min)	Ultra-Turrax 10000 (1min)
<b>Emu O/W 3.1</b>	0.75 (5.2 wt%)	14.25 (94.7wt%)	7.5 (0.05 wt%)	Ultra-Turrax 4000 (5 min)	Ultrasound bath (2 min 40kHz) + Handshaking (1 min)
<b>Emu O/W 4</b>	0.75 (5 wt%)	14.25 (95 wt%)	45 (0.3 wt%)	Ultra-Turrax 4000 (5 min)	Ultrasound bath (2 min 40kHz) + Handshaking (1 min)
<b>Emu O/W 5</b>	1.5 (10.5 wt%)	12.75 (89.3 wt%)	15 (0.1 wt%)	Ultra-Turrax 4000 (5 min)	Ultrasound bath (2 min 40kHz) + Handshaking (1 min)
<b>Emu O/W 5.1</b>	1.5 (10.5 wt%)	12.75 (89.4wt%)	15 (0.1 wt%)	Ultra-Turrax 4000 (5 min)	Ultrasound bath (2 min 40kHz) + Ultraturrax 10000 (1 min)
<b>Emu O/W 5.2</b>	1.5 (10.5 wt%)	12.75 (89.4wt%) (pH 3)	15 (0.1 wt%)	Ultra-Turrax 4000 (5 min)	Ultrasound bath (2 min 40kHz) + Handshaking (1 min)

835

836

837 **Table 4:**  $^{13}\text{C}$  chemical shifts of signals C2 and C2' for the three known curcumin polymorphs (Dai et al., 2020).

$^{13}\text{C}$ CPMAS SSNMR – Chemical shift ( $\delta$ , ppm)			
	<i>Form I</i>	<i>Form II</i>	<i>Form III</i>
<b>C2</b>	187.4	189.6	190.2
		186.2	
<b>C2'</b>	182.7	179.2	177.8
		177.8	

838

839

840

841 **Table 5:** Attachment energy calculation, surface roughness and percentage areas of the most dominant  
 842 facets relative both to curcumin polymorphs form I and form III.

	hkl	dhkl	Eatt (Total) (kcal mol <sup>-1</sup> )	Eatt (vdW) (kcal mol <sup>-1</sup> )	Eatt (Electrostatic) (kcal mol <sup>-1</sup> )	Eatt (H-bond) (kcal mol <sup>-1</sup> )	% Total facet area	Roughness
<b>Form I</b>	{101}	11.11	-63.9	-61.3	0	-2.6	5.1	1.244
	{101}	10.25	-26.8	-25.5	0	-1.3	42.4	1.196
	{002}	9.92	-40.8	-39.5	0	-1.3	24.2	1.780
	{010}	7.18	-45.3	-44.3	0	-1.0	23.1	1.627
<b>Form III</b>	{002}	17.23	-104.3	-61.5	-27.6	-15.2	30.7	1.686
	{102}	10.14	-130.5	-67.1	-27.6	-35.9	35.2	2.980
	{111}	6.61	-178.4	-113.5	-36.7	-28.3	34.1	1.693

843

844

845

**Table 6:** The contact angle values for raw curcumin and recrystallized curcumin are reported. Water at pH 7, pH 3 (adjusted with HCl 0.1M) and MCT oils were tested.

	<b>Water (<math>\theta_1</math> pH 7)</b>	<b>Water (<math>\theta_1</math> pH 3)</b>	<b>Oil (<math>\theta_2</math>)</b>
<b>Cur Raw (Form I)</b>	90.0° ± 5.0°	84.3° ± 10.3°	29.0° ± 0.7°
<b>Cur (Form III)</b>	62.4° ± 6.4°	63.3° ± 1.9°	24.4° ± 2.5°

846

847

848

849

850

851

852

**Table 7:** Mean droplet size (diameter) and standard deviation (S.D.) calculated from images analysis using ImageJ software, as reported above for particle size distribution. The wide range of dimensions is due to the formation of smaller droplets which create a nest that stabilize bigger droplets through bridging mechanism.

	Mean ( $\mu\text{m}$ )	S.D. ( $\mu\text{m}$ )
<b>1</b>	68.83	38.07
<b>2</b>	51.75	38.97
<b>3</b>	60.45	27.48
<b>4</b>	78.40	38.01
<b>5</b>	77.16	39.46
<b>6</b>	75.64	30.68
<b>7</b>	87.32	53.78
<b>8</b>	81.52	46.26
<b>9</b>	71.75	60.09
<b>10</b>	95.74	61.86
<b>11</b>	97.60	40.81
<b>12</b>	97.13	54.04
<b>13</b>	119.20	109.77
<b>14</b>	100.44	82.05
<b>15</b>	114.11	103.88
<b>16</b>	115.81	106.89

853